



ELSEVIER

Combustion and Flame 132 (2003) 25–33

Combustion
and Flame

Effects of structure and hydrodynamics on the sooting behavior of spherical microgravity diffusion flames

P.B. Sunderland^a, R.L. Axelbaum^{b,*}, D.L. Urban^c, B.H. Chao^d, S. Liu^d

^aNational Center for Microgravity Research, Cleveland, OH 44135, USA

^bDepartment of Mechanical Engineering, Washington University, St. Louis, MO 63130, USA

^cNASA Glenn Research Center, Cleveland, OH 44135, USA

^dDepartment of Mechanical Engineering, University of Hawaii, Honolulu, HI 96822, USA

Received 29 May 2001; received in revised form 12 June 2002; accepted 27 June 2002

Abstract

This study is an examination of the sooting behavior of spherical microgravity diffusion flames burning ethylene at atmospheric pressure in a 2.2-s drop tower. In a novel application of microgravity, spherical flames were employed to allow convection across the flame to be either from fuel to oxidizer or from oxidizer to fuel. Thus, spherical microgravity flames are capable of allowing stoichiometric mixture fraction, Z_{st} , and direction of convection across the flame to be controlled independently. This allowed for a study of the phenomenon of *permanently blue* diffusion flames—flames that remain blue as strain rate approaches zero. Z_{st} was varied by changing inert concentrations such that adiabatic flame temperature did not change. At low Z_{st} , nitrogen was supplied with the oxidizer, and at high Z_{st} , it was provided with the fuel. Flame structure, quantified by Z_{st} , was found to have a profound effect on soot production. Soot-free conditions were observed at high Z_{st} and sooting conditions were observed at low Z_{st} , regardless of convection direction. Convection direction was found to have a smaller impact on soot inception, suppressing formation when convection at the flame sheet was directed towards the oxidizer. A numerical analysis was developed to simulate steady state conditions and aided the interpretation of the results. The analysis revealed that steady state was not achieved for any of the flames, but particularly for those with pure ethylene or oxygen flowing from the porous burner. Furthermore, despite the fact that all flames had the same adiabatic flame temperature, the actual peak temperatures differed considerably. While transient burner heating and burner radiation reduced flame temperature, gas-phase radiative heat loss was the dominant mechanism accounting for these differences. © 2003 The Combustion Institute. All rights reserved.

Keywords: Soot; Spherical flames; Microgravity; Oxygen-enhanced combustion; Inverse flames

1. Introduction

Recent experimental, numerical, and analytical work has shown that stoichiometric mixture fraction, Z_{st} , [1] (defined as the mixture fraction where the fuel and oxidizer are in stoichiometric proportions for

given fuel and oxidizer freestream concentrations) can have a profound effect on soot formation in counterflow diffusion flames [2–8]. This effect appears even at constant adiabatic flame temperature (T_{ad}), as demonstrated by Du and Axelbaum [2,3]. At high Z_{st} , flames of most hydrocarbons remain blue when the strain rate approaches zero in counterflow flames, or as flame height and residence time approach infinity in coflowing flames. Lin and Faeth [5] coined the term *permanently blue* to describe such flames.

* Corresponding author. Tel.: +1-314-935-7560; fax: +1-314-935-4014.

E-mail address: rla@mecf.wustl.edu (R.L. Axelbaum).

Nomenclature**Roman characters**

c_p	specific heat at constant pressure
d	diameter
G_{Rb}	radiative heat transferred from gas to burner
m	mass flow rate
Nu	Nusselt number
Pe	Peclet number
Q_r	radiative loss as a fraction of heat release
q_1	heat of combustion per unit mass of burner reactant
R	radiation intensity
r	radial coordinate
r_e	radius bounding radiating gas region
T	temperature
u	velocity
W	molecular weight
X	mole fraction
Y	mass fraction
Z	mixture fraction

Greek

α	weighting factor
ε	effective emissivity of the burner
φ	burner porosity
κ	Planck mean absorption coefficient
λ	thermal conductivity
ν	stoichiometric coefficient
ρ	density
σ	Stefan-Boltzmann constant

Superscript

\sim non-dimensional quantity

Subscripts

ad	adiabatic
b	burner surface
<i>corrected</i>	corrected for radiation
f	flame sheet or luminous boundary
g	gas
i	inner surface of the burner
<i>raw</i>	not corrected for radiation
s	burner material
st	stoichiometric
0	condition at $r = 0$
1	burner reactant
2	ambient reactant
∞	condition at $r \rightarrow \infty$

Past studies have attributed the primary cause of permanently blue conditions to either structure [2,4] or hydrodynamics [5–8], although these studies typically noted the importance of both factors. The *structural* effect refers to the variations in species concentration and temperature profiles in mixture fraction space that are a direct consequence of changes in Z_{st} . On the other hand, the *hydrodynamic* effect, as defined here, refers to the effect that occurs due to the direction that the soot or soot precursors are being convected—either into the oxidizer or into the fuel.

As shown below, when Z_{st} is varied the effects of structure and hydrodynamics cannot be independently studied in normal gravity flames. Fig. 1 illustrates the hydrodynamic effect for counterflow flames. When fuel and oxidizer are chosen such that $Z_{st} < 0.5$ (Fig. 1a), the flame is on the oxidizer side of the stagnation plane and the flow across the flame is directed towards the fuel. Newly formed soot is convected into richer regions, favoring soot growth over oxidation. On the other hand, when $Z_{st} > 0.5$ (Fig. 1b) the flame is on the fuel side and convection at the flame is towards the oxidizer. In this case, hydrodynamics drives the soot towards the oxidizer, thereby retarding soot formation. Thus, when the structure is changed (e.g., Z_{st} is increased) the influence of hydrodynamics changes as well.

Du and Axelbaum (Ref. 2 comment and reply) proposed that while soot growth and oxidation are affected by the direction of convection, it is soot inception that dictates permanently blue conditions. Soot growth and oxidation depend on the existence of soot particles, whereas soot-particle inception arises from gas-phase reactions. While particles have relatively small diffusion velocities and tend to follow streamlines, gaseous species diffuse more readily. Thus, inception is not expected to depend strongly on flow direction. For example, there is no abrupt change in the flame response when it moves across the stagnation plane [3]. The flame is a diffusive-convective system and this balance allows for changes in convection direction without substantial changes in flame response. Furthermore, it is possible to produce soot in counterflow flames when $Z_{st} > 0.5$ even though convection drives particles into the oxidizer [2,5].

The structural explanation for permanently blue flames is illustrated in Fig. 2. The fuel, oxygen and temperature distributions in Z (mixture fraction) space are depicted for an ethylene/air flame ($Z_{st} = 0.064$) in Fig. 2a, and for a diluted ethylene/oxygen flame ($Z_{st} = 0.78$) in Fig. 2b. The flame sheet approximation is shown, but dashed lines delineate the high-temperature region available for soot reactions. Flames with larger Z_{st} have lower fuel concen-

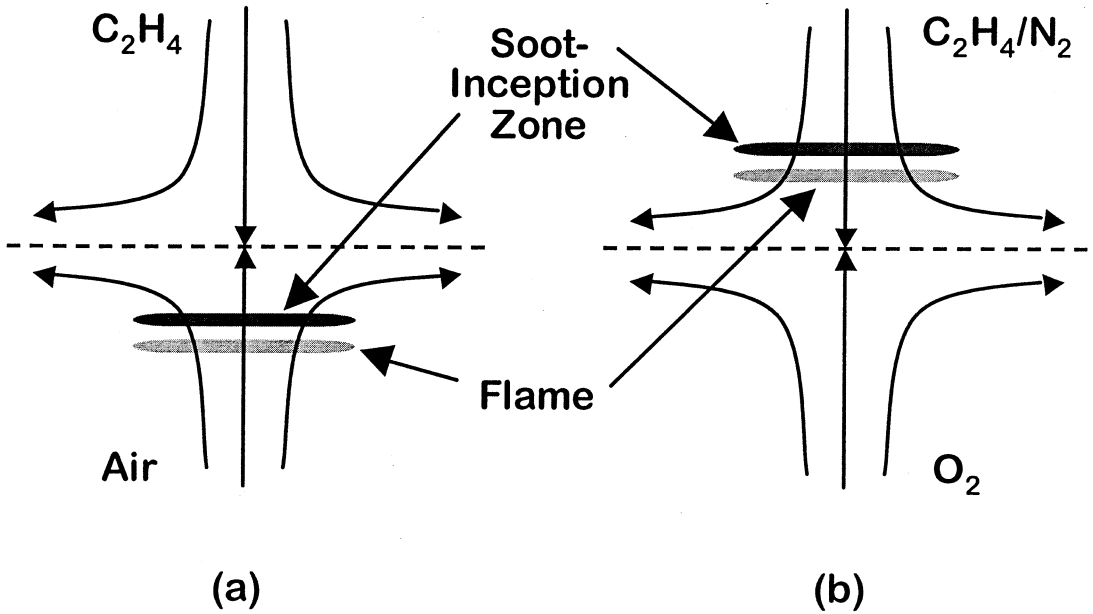


Fig. 1. Schematic representation of counterflow flames with (a) $Z_{st} < 0.5$ where the flame is on the oxidizer side of the stagnation plane and (b) $Z_{st} > 0.5$ where the flame is on the fuel side of the stagnation plane. Soot inception occurs under fuel rich conditions and (neglecting thermophoresis) the particles are convected with the flow.

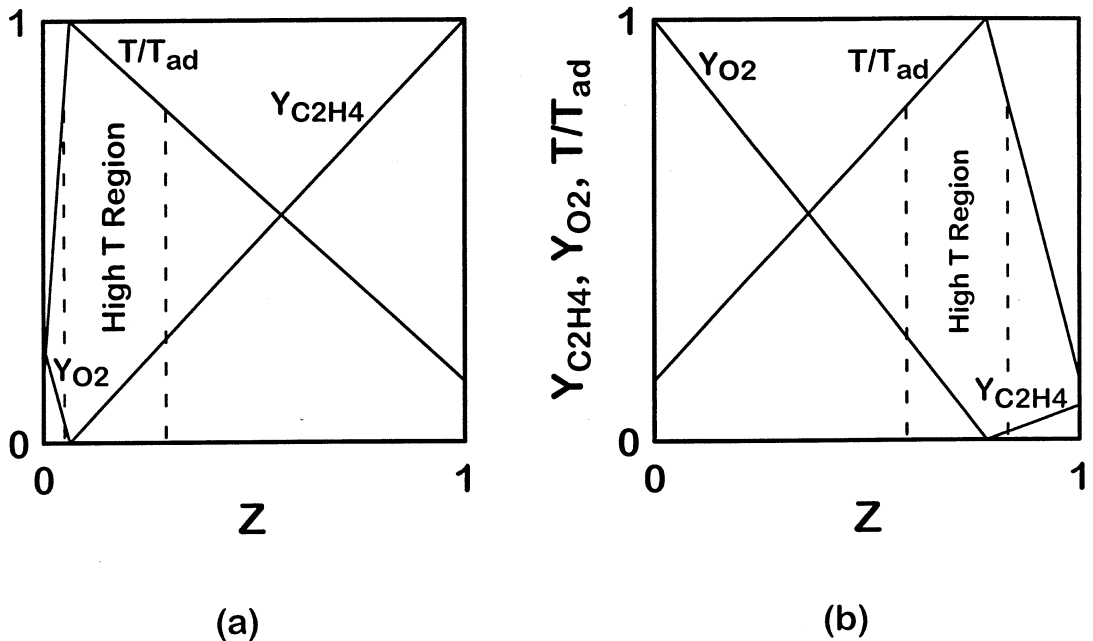


Fig. 2. Representation of normalized temperature and fuel and oxidizer mass fractions versus mixture fraction for diffusion flames with (a) $Z_{st} = 0.064$ and (b) $Z_{st} = 0.78$. The dashed lines demarcate a high temperature zone. Reproduced from Du and Axelbaum [2].

trations and higher oxygen concentrations in the high temperature zone, as well as a shift in the O_2 and OH profiles towards the fuel side of the flame [2]. Be-

cause the presence of O_2 and OH retards precursor growth [9], this shift can dramatically reduce soot inception by narrowing the soot-inception zone.

Table 1
Test conditions and flame measurements

Flame	Ambient	Prescribed				Measured		
		$X_{C_2H_4}$	X_{O_2}	Z_{st}	m_b , mg/s	d_j , mm	T_{raw} , K	$T_{corrected}$, K
a	Oxidizer	1	0.21	0.064	1.51	29.3	1302	1399
b	Oxidizer	0.08	1	0.78	18.6	18.8	1760	1923
c	Fuel	1	0.21	0.064	22.2	24.7	1907	2111
d	Fuel	0.08	1	0.78	5.18	31.3	1300	1385

From this perspective, permanently blue conditions are realized when significant oxidizing species are on the fuel side in the region where temperatures are above the threshold temperature for soot inception, 1250 to 1650 K at moderate pressures [10–13]. For such flames, in regions where temperatures are high enough to produce soot, there is sufficient oxidizer to consume the soot precursors. Consumption overcomes production and, in this respect, the soot formation region for high Z_{st} flames resembles that of a soot-free premixed flame.

Previous studies of permanently blue flames have involved counterflow and gas-jet configurations, which do not allow independent variation of flame structure and convection direction. Thus, it was not possible to assess the relative contributions of structure and hydrodynamics because both mechanisms suppress soot formation at high Z_{st} in normal-gravity diffusion flames. In this study, we employ spherical diffusion flames to address this problem. The unique properties of spherical diffusion flames have attracted much attention. Their structure has been considered theoretically by Buckmaster and Ludford [14], Williams [1], and Mills and Matalon [15]. Studies of spherical flames typically have involved droplet combustion in microgravity [16–18], although flames supported by porous spheres in normal gravity [19] and in microgravity [20] have been considered as well. Because steady-state spherical diffusion flames are one-dimensional and strain-free they hold great utility for studies of soot formation.

In this work we consider the sooting behavior of four spherical flames with the same ethylene consumption rates and T_{ad} . We altered structure by exchanging inert between the oxidizer and the fuel. We independently varied the direction of convection across the flame sheet by interchanging the injected and ambient gases.

2. Experimental

The microgravity experiments were conducted in the NASA Glenn 2.2-s drop tower using a general-

purpose combustion rig. The rig includes a windowed pressure vessel supported by a fuel-delivery system, an ignitor, a color CCD camera, a microprocessor controller and lead-acid batteries. The burner is a 6.4 mm diameter porous sphere consisting of sintered 10 micron stainless steel particles. The sphere is supported and fed by a 1.6 mm stainless steel tube attached with epoxy. The sphere is positioned at the center of the cylindrical chamber, whose diameter, length and volume were 25 cm, 53 cm, and 26 liters, respectively. All tests were conducted in quiescent ambient gas at 0.98 bar.

The tests employed the following gases: ethylene, oxygen, synthetic air (0.21 mole fraction oxygen in nitrogen), and diluted ethylene (0.0814% ethylene by volume in nitrogen). Purities of the nitrogen and oxygen were 99.999% while that for ethylene was 99.9%. Nitrogen mixtures were purchased, having been prepared by gravimetric mixing to within 0.02% of the reported compositions. The burner feed gas was stored at 8 bar in a 75 mL bottle aboard the rig and was delivered via a pressure regulator, a solenoid valve, a fine-needle valve, a calibrated mass-flow meter, and a second solenoid valve. Burner flow rates were established before ignition. Uncertainties in the flow-rates (at the 95% confidence level) are estimated at 5%. Before each test, two purges of the chamber were performed by evacuating the chamber to 0.03 bar and filling to 0.98 bar with the appropriate ambient gas.

Microgravity laminar flames are sensitive to hydrodynamic disturbances, such as those caused by ignition before entry into microgravity, retracting ignitors, and ignition deflagrations. To minimize these disturbances, the flames were ignited immediately after release into microgravity using a spring-loaded Nichrome wire (length of 12 mm and diameter of 0.36 mm). The ignitor wire was energized at 28 VDC, whereby it quickly glowed and ruptured. Immediately thereafter, both ends retracted with minimal wakes. The serial pair of solenoid valves facilitated smooth ignition via optimization of the initial gas discharge.

The four flames considered, as summarized in Table 1, are: (a) ethylene issuing into air, (b) diluted

ethylene issuing into oxygen, (c) air issuing into ethylene, and (d) oxygen issuing into diluted ethylene. Z_{st} is 0.064 in flames (a) and (c), and 0.78 in flames (b) and (d). The convection direction is from fuel to oxidizer in flames (a) and (b) and from oxidizer to fuel in flames (c) and (d). The ethylene consumption rate for all flames was held constant at 1.51 mg/s, yielding the burner mass flowrates shown in Table 1. Under the assumptions of equal diffusivities of all species and heat these flames have identical nitrogen concentrations at their stoichiometric contours and their adiabatic flame temperatures are the same, $T_{ad} = 2370$ K.

The flames were imaged through the chamber window using a color CCD camera. A 16 mm fixed-iris lens was used, with apertures (f 1.4–8) chosen according to flame luminosity. Video signals were carried via fiber-optic cable to a stationary color S-VHS video recorder. Digitized images were subsequently obtained from the tapes using a framegrabber. Spatial resolution in the video images was 0.3 mm. Soot formation in diffusion flames commences at 1250 to 1650 K [10–13], well above the minimum temperature at which soot emits visible light. Thus, diffusion flames that create soot necessarily emit yellow luminosity, and experiments have shown that the onset of yellow emissions is an effective means of determining soot inception limits in hydrocarbon diffusion flames [21]. Testing in normal gravity has confirmed our video system to be sensitive to the presence of even trace quantities of soot in flames.

Gas-phase temperatures were measured with an uncoated B-type thermocouple with a wire diameter of 51 μm and a butt-welded junction of the same diameter. The thermocouple supports were 20 mm apart to minimize disturbances. The thermocouple was positioned to be tangential to the flames and was held in a fixed position for each test so that the slowly expanding flame passed the junction approximately 0.2 s before drop termination. The thermocouple response was monitored at 300 Hz and the temperatures were recorded.

The gas-phase temperatures were obtained by correcting for the radiative loss from the thermocouple. To do this the radiative loss from the thermocouple was balanced against the convective heating of the thermocouple assuming steady state conditions. The thermocouple was assumed to radiate as a graybody with an emissivity of 0.2 [22]. The heat transfer coefficient was obtained from the relationship of Nakai and Okazaki [23],

$$Nu = [0.8237 - \ln(Pe/2)]^{-1} \quad \text{for } Pe < 0.2, \quad (1)$$

where Nu and Pe were based on the wire diameter and transport properties of nitrogen at the average of

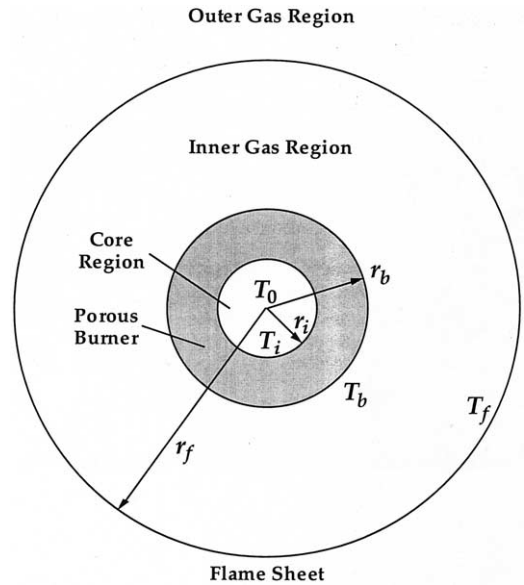


Fig. 3. Schematic of a spherical diffusion flame as represented by the analytical model.

the thermocouple and gas temperatures. To identify Pe required specifying a local velocity and this was estimated based on steady-state conservation of mass from the burner to the flame, where a molecular weight of 28 g/mole was assumed. Nu was found to range from 0.21 to 0.33 with a relatively weak dependence on Pe . The corrected temperature measurements have estimated uncertainties (at the 95% confidence level) of ± 50 K.

3. Model

An analytical model was developed to help interpret the observed flame sizes, flame transients, and peak temperatures. The model assumes steady and nonbuoyant conditions, spherical symmetry, unity Lewis number, a single-step reaction and three sources of radiation: the burner surface, CO_2 , and H_2O . The burner is assumed to be a graybody for radiative absorption and emission. Gas radiation involves optically thin conditions. Soot radiation is neglected here, as discussed below. Mass diffusivity, $c_{p,g}$ and λ_g are allowed to vary between flames but are assumed constant for a given flame. This model follows the previous models of nonbuoyant spherical flames [20,24,25].

The burner gas is assumed to be supplied from a point source with a temperature of T_0 . The flow domain is split into four regions as depicted in Fig. 3: a core region before the gas reaches the porous burner, a burner region in which the gas passes through the burner, an inner gas region between the

burner and the flame sheet, and an outer gas region outside the flame sheet. Under the flame-sheet approximation, there is only one reactant in each region. The gas and solid temperatures at a given radius within the burner are assumed to be equal.

Based on the above considerations, the nondimensional energy conservation equation in each region is given by:

core region:

$$\frac{d}{d\tilde{r}} \left(\tilde{m}\tilde{T} - \tilde{r}^2 \frac{d\tilde{T}}{d\tilde{r}} \right) = 0, \quad (2)$$

burner region:

$$\frac{d}{d\tilde{r}} \left(\tilde{m}\tilde{T} - \tilde{\lambda}_s \tilde{r}^2 \frac{d\tilde{T}}{d\tilde{r}} \right) = 0, \quad (3)$$

inner and outer gas regions except at the flame sheet:

$$\frac{d}{d\tilde{r}} \left(\tilde{m}\tilde{T} - \tilde{r}^2 \frac{d\tilde{T}}{d\tilde{r}} \right) = -4R\tilde{r}^2 \tilde{\kappa} (\tilde{T}^4 - \tilde{T}_\infty^4). \quad (4)$$

The symbols used here and below are defined in the Nomenclature section above. Equations 2–4 are solved subject to the following boundary and interface conditions:

$$\tilde{r} = 0: \tilde{T} = \tilde{T}_0, \quad (5)$$

$$\tilde{r} = \tilde{r}_i: \tilde{T} = \tilde{T}_i, \quad (d\tilde{T}/d\tilde{r})_{\tilde{r}_i^-} = \tilde{\lambda}_s (d\tilde{T}/d\tilde{r})_{\tilde{r}_i^+}, \quad (6)$$

$$\begin{aligned} \tilde{r} = 1: \tilde{T} = \tilde{T}_b, \quad \tilde{\lambda}_s \left(\frac{d\tilde{T}}{d\tilde{r}} \right)_{1^-} \\ = \left(\frac{d\tilde{T}}{d\tilde{r}} \right)_{1^+} + \varepsilon [G_{Rb} - R(\tilde{T}_b^4 - \tilde{T}_\infty^4)], \end{aligned} \quad (7)$$

$$\tilde{r} = \tilde{r}_f: (d\tilde{T}/d\tilde{r})_{\tilde{r}_f^+} = (d\tilde{T}/d\tilde{r})_{\tilde{r}_f^-} - (\tilde{m}/\tilde{r}_f^2), \quad (8)$$

$$\tilde{r} \rightarrow \infty: \tilde{T} \rightarrow \tilde{T}_\infty, \quad (9)$$

where T_i and T_b are to be determined, and

$$G_{Rb} = 2R \int_1^{\tilde{r}_e} \tilde{\kappa} \tilde{r}^2 (\tilde{T}^4 - \tilde{T}_b^4) [1 - (1 - \tilde{r}^{-2})^{1/2}] d\tilde{r} \quad (10)$$

and $[1 - (1 - \tilde{r}^{-2})^{1/2}]/2$ represents the fraction of radiative emission that reaches the burner surface.

The following nondimensional quantities are defined:

$$\tilde{T} = \frac{c_{p,g} T}{q_1 Y_{1,0}}, \quad \tilde{Y}_1 = \frac{Y_1}{Y_{1,0}}, \quad \tilde{Y}_2 = \frac{\nu_1 W_1}{\nu_2 W_2} \frac{Y_2}{Y_{1,0}},$$

$$\tilde{r} = \frac{r}{r_b}, \quad \tilde{\kappa} = r_b \kappa, \quad \tilde{m} = \frac{c_{p,g} m}{4\pi r_b \lambda_g},$$

$$\tilde{\lambda}_s = \varphi + (1 - \varphi) \frac{\lambda_s}{\lambda_g}, \quad R = \frac{\sigma r_b}{\lambda_g} \left(\frac{q_1 Y_{1,0}}{c_{p,g}} \right)^3, \quad (11)$$

where $m = 4\pi r^2 \rho_g u$ is the constant mass flow rate of the gas and $\kappa = X_{\text{CO}_2} \kappa_{\text{CO}_2} + X_{\text{H}_2\text{O}} \kappa_{\text{H}_2\text{O}}$. The values of κ_{CO_2} and $\kappa_{\text{H}_2\text{O}}$ are adopted from Abu-Romia and Tien [26].

The species conservation equations are solved following the conventional approach adopted in droplet combustion [27] and yield:

core and burner regions:

$$\tilde{Y}_1 = 1, \quad \tilde{Y}_2 = 0, \quad (12)$$

inner gas region:

$$\tilde{Y}_1 = 1 - (1 + \tilde{Y}_{2,\infty}) \exp(-\tilde{m}/\tilde{r}), \quad \tilde{Y}_2 = 0, \quad (13)$$

outer gas region:

$$\tilde{Y}_1 = 0, \quad \tilde{Y}_2 = (1 + \tilde{Y}_{2,\infty}) \exp(-\tilde{m}/\tilde{r}) - 1. \quad (14)$$

The stoichiometric flame sheet is located at

$$\tilde{r}_f = \tilde{m}/\ell n(1 + \tilde{Y}_{2,\infty}). \quad (15)$$

The model was exercised for the four test flames, using the following fixed parameters:

$$r_i = 0.16 \text{ cm}, \quad r_b = 0.32 \text{ cm}, \quad \varphi = 0.5,$$

$$\begin{aligned} T_0 = T_\infty = 300 \text{ K}, \quad q_1 = 47160 \text{ J/g}, \quad m_{\text{C}_2\text{H}_4} \\ = 1.51 \text{ mg/s}, \end{aligned}$$

$$W_{\text{C}_2\text{H}_4} = 28.0 \text{ g/mole}, \quad \nu_{\text{C}_2\text{H}_4} = 1.0,$$

$$W_{\text{O}_2} = 32.0 \text{ g/mole}, \quad \nu_{\text{O}_2} = 3.0,$$

$$c_{p,s} = 0.46 \text{ J/(g}\cdot\text{K)}, \quad \lambda_s = 30 \text{ W/(m}\cdot\text{K)}, \quad \varepsilon = 0.4.$$

The parameters that were varied included λ_g , $c_{p,g}$, κ_{CO_2} and $\kappa_{\text{H}_2\text{O}}$. Appropriate mean values for $c_{p,g}$ and λ_g were determined using the relation $T = T_b + \alpha(T_f - T_b)$ with $\alpha = 0.8$, adopting here the properties of air. Recognizing the sensitivity of radiation to temperature, the Planck mean absorption coefficients were evaluated at a higher temperature of $\alpha = 0.9$. Because the burner and flame temperatures were not known a priori, the computations were performed iteratively until the transport properties converged.

4. Results and discussion

Fig. 4 shows color images, captured just before drop termination, of representative flames for the four conditions considered. At least 10 flames were observed at each condition to confirm repeatability. Additionally, tests at other flowrates confirmed that the observations were not significantly affected by

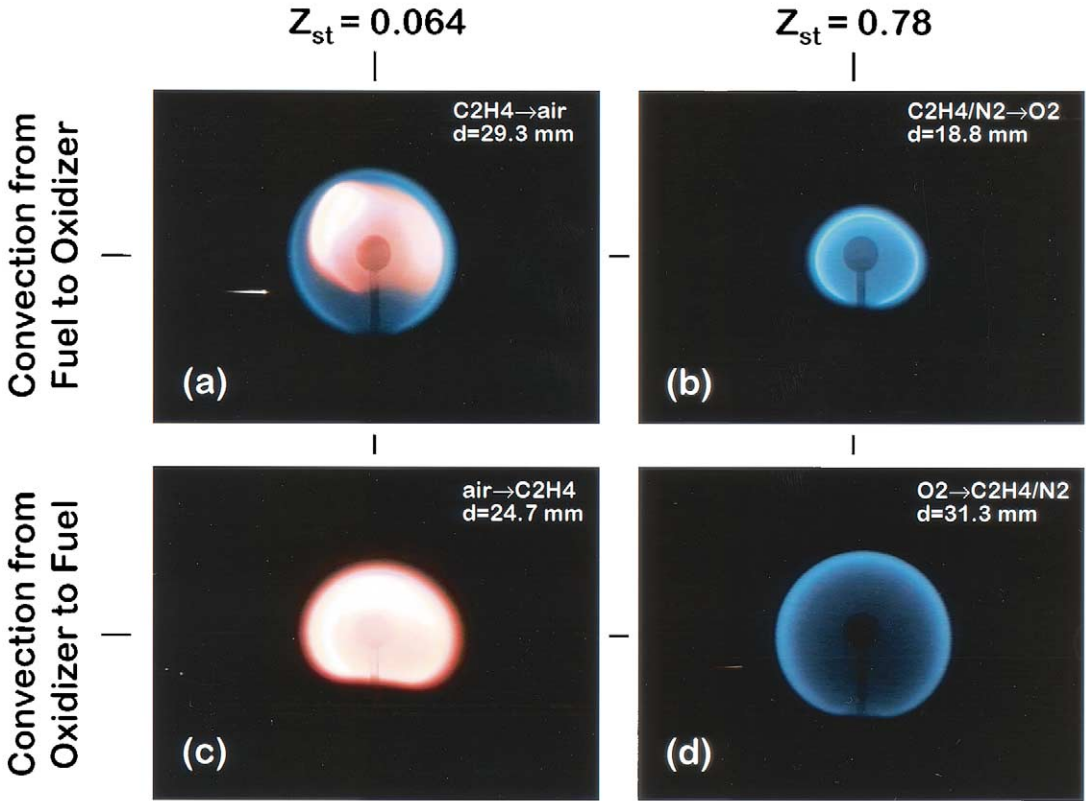


Fig. 4. Color images of representative flames at the end of the 2.2 s drop for flames (a–d): (a) ethylene issuing into air, f1.4, (b) diluted ethylene issuing into oxygen, f4, (c) air issuing into ethylene, f8, (d) oxygen issuing into diluted ethylene, f1.4. The scale is revealed by the 6.4-mm spherical burner. The ethylene consumption rate is 1.51 mg/s in all cases.

flowrate. Flame (a) involves ethylene burning in air and has a yellow interior surrounded by a well-defined blue flame. Flame (b) involves diluted ethylene issuing into ambient oxygen, and is bright blue. Flame (c) considers air issuing into ethylene, and is yellow and the brightest of the four flames. Finally, flame (d) involves oxygen issuing into diluted ethylene, and it has a dim, diffuse blue interior surrounded by a bright blue sheet. Flames (b–d) had little color variation throughout the 2.2 s tests while flame (a) displayed a slowly decreasing yellow luminosity.

The final diameters of the present flames are tabulated in Table 1. Diameters were determined by averaging the longest chord through a flame and its perpendicular chord. Recalling that the flames have the same ethylene consumption rate, flames (b) and (c) are smaller than the others since they involve diluted burner gas and pure ambient gas. The temporal variation of luminous flame diameter for the four flames is shown in Fig. 5, where time is defined to be zero at ignition. Immediately after ignition a pre-mixed deflagration wave propagated outward after which the flames contracted into non-premixed con-

ditions. From 0.2 s until drop termination, the flames grew monotonically. This transient behavior is re-

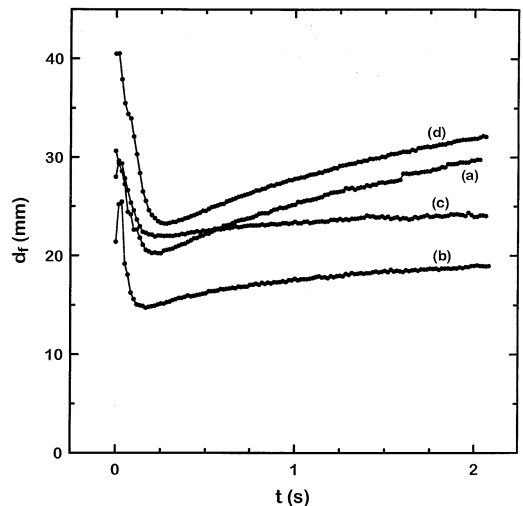


Fig. 5. Variation of flame luminous diameter with time for flames (a–d).

Table 2
Model results

Flame	λ_g W/m · K	$c_{p,g}$ J/g · K	κ_{CO_2} cm ⁻¹	$\kappa_{\text{H}_2\text{O}}$ cm ⁻¹	d_f mm	T_f K	$Q_{r,f}$	$Q_{r,b}$
a	0.045	1.046	0.403	0.173	85.1	630	0.89	3.5×10^{-4}
b	0.087	1.212	0.119	0.0204	26.5	1654	0.45	1.6×10^{-4}
c	0.116	1.307	0.0484	0.0099	14.4	2270	0.14	5.4×10^{-4}
d	0.048	1.058	0.413	0.140	74.2	694	0.86	1.4×10^{-4}

duced when nitrogen is supplied through the burner [flames (b) and (c)] because of decreased residence times.

The peak temperatures of the four flames measured near the end of the drop are tabulated in Table 1 in both raw and radiation-corrected forms. Despite the uniform $T_{ad} = 2370$ K and ethylene consumption rates, the flames have disparate peak temperatures, as discussed below.

Fig. 4 reveals that the sootiest flame is flame (c), with air injecting into ethylene. This is expected since both flame structure (small Z_{st}) and convection direction (towards fuel) promote soot formation and the peak temperature is the highest. Conversely, one would expect the least soot in flame (b) because it has a large Z_{st} , its convection is towards the oxidizer, and its temperature is lower. Indeed, flame (b) is soot free.

The effect of convection direction on soot formation at constant Z_{st} is observed in flames (a) and (c). These flames both have $Z_{st} = 0.064$ (favoring soot formation) but opposite convection directions. Particles formed in flame (a) are convected towards the oxidizer where they appear to completely oxidize. The presence of yellow luminosity in flame (a) suggests that convection into the oxidizer suppresses soot growth but does not eliminate soot inception. Flame (c) has a high flame temperature and the soot particles formed at the flame are convected towards the fuel, allowing for remarkable soot growth.

The effect of flame structure (Z_{st}) on soot formation is most apparent in flame (d), where convection is directed towards the fuel (favoring soot formation). Structure is seen to have a significant effect, yielding a blue flame at $Z_{st} = 0.78$. Blue flame conditions are realized in flame (d) despite the fact that convection is towards the fuel, which would suggest favorable conditions for soot growth. Flames (a) and (d) allow for a clear indication of the relative importance of structure and convection direction on the phenomena of permanently blue flames. The flames have almost identical peak temperatures but convection favors soot oxidation in flame (a) and soot formation in flame (d). Flame (a) produces soot while flame (d) does not, indicating that flame structure is responsible

for the soot free conditions of flame (d). Furthermore, flame (b), with $Z_{st} = 0.78$ and a temperature of 1923 K, is soot free. These results attest to the dramatic effects of Z_{st} on soot inception.

Insights into the observed flame development, flame size, and peak temperature can be gained from the present analytical model. The numerical iteration discussed above led to the values of λ_g , $c_{p,g}$, κ_{CO_2} , and $\kappa_{\text{H}_2\text{O}}$ as shown in Table 2. Table 2 also shows the steady-state model predictions for d_f and T_f . There is considerable discrepancy between the experimental results in Table 1 and the results for the steady state model in Table 2. An explanation for the differences is proposed below.

The predicted flame diameters in Table 2 and the results of Fig. 5 lend confirmation that flames (a) and (d) have not reached steady sizes within 2.2 s. The predicted flame diameters are considerably larger than the diameters measured at 2.2 s. These flames have low volumetric flowrates and long residence times, resulting in a slow evolution. The predicted diameter of flame (b) indicates that this flame is relatively close to steady size owing to its short residence time. The predicted diameter of flame (c) is lower than measured. This is believed to be due to the fact that what is being experimentally measured for flame (c) is not the flame but the edge of the hot soot zone. Thus the actual flame location should be smaller than the yellow luminous zone observed. Temperature predictions also indicate that flames (a) and (d) have not reached steady state within 2.2 s. The low predicted temperatures are attributed to increased radiation associated with the larger sizes of the steady state flames. Moreover, the predictions suggest that flames (a) and (d) may extinguish before reaching steady conditions. (The model assumes a flame sheet and, thus, cannot predict extinction.) The measured temperatures of flames (b) and (c) are closer to their steady-state predictions because these flames are close to their steady-state sizes. The over-prediction of T_f for flame (c) is attributed to the absence of soot radiation in the analytical model. Despite this, the model and experiment agree reasonably well for flame (c) and as suggested from Fig. 5, this flame is near steady state.

At steady state the measured peak temperatures can fall below $T_{ad} = 2370$ K owing to two main loss mechanisms: radiation from the gas and soot, and radiation from the burner. Table 2 reveals that in steady state $Q_{r,f}$ is much larger than $Q_{r,b}$ for all four flames, indicating that burner radiation is negligible even in steady state. The present analysis also indicates that the large variation in peak temperatures between flames that have the same T_{ad} is primarily due to gas radiation. Gas radiation is smaller for flames (b) and (c) than for the other flames owing to their small flame sizes and residence times. This is most dramatic for flame (c), which is nearly devoid of radiative losses in the present soot-free model.

5. Conclusions

Four configurations of spherical microgravity diffusion flames were observed in the NASA Glenn 2.2 s drop tower, and a supporting model was developed. The conditions are uniquely suited to studying permanently blue flames because they allow independent variation of structure and convection direction. Flames with $Z_{st} = 0.78$ were soot-free and flames with $Z_{st} = 0.064$ appeared yellow regardless of convection direction. For the flames with low Z_{st} , less soot was evident when convection was towards the oxidizer, but permanently blue conditions were not realized.

Experimental and numerical results indicate that these flames did not reach steady state within the available 2.2 s of microgravity. Furthermore, while all the flames had identical T_{ad} , the measured and predicted peak temperatures varied widely. Numerical results indicate that the differences are due primarily to differences in gas-phase radiation. Despite these limitations, it was possible to compare flames with nearly equal temperatures but different convection directions and Z_{st} . The results indicate that permanently blue flames owe their existence more to flame structure than to convection direction.

An important ancillary result of this work is the demonstration of a unique application of microgravity that should have applications beyond this study. That is, the direction of convection across the flame can be reversed for a given fuel and oxidizer. Thus, microgravity affords a new level of control and a unique tool for studying diffusion flames.

Acknowledgment

This work was supported by NASA Grants NCC3-697 and NAG3-1910 (RLA), and NCC3-696a

and NAG3-1912 (BHC), with D.P. Stocker serving as Project Scientist. The assistance of S.A. Gokoglu, C.B. Lundquist, J.E. Pierce, and H.D. Ross is duly appreciated.

References

- [1] F.A. Williams, *Combustion Theory*. Benjamin/Cummings, Menlo Park, 1985, pp. 55 and 75.
- [2] J. Du, R.L. Axelbaum, *Combust. Flame* 100 (1995) 367.
- [3] J. Du, R.L. Axelbaum, *Proc. Combust. Inst.* 26 (1996) 1137.
- [4] B.H. Chao, S. Liu, R.L. Axelbaum, *Comb. Sci. Tech.* 138 (1998) 105.
- [5] K.-C. Lin, G.M. Faeth, *J. Prop. Power* 12 (1996) 691.
- [6] K.-C. Lin, G.M. Faeth, *J. Prop. Power* 12 (1996) 10.
- [7] K.-C. Lin, G.M. Faeth, *Combust. Flame* 115 (1998) 468.
- [8] G. Sugiyama, *Proc. Combust. Inst.* 25 (1994) 601.
- [9] P. Markatou, H. Wang, M. Frenklach, *Combust. Flame* 93 (1993) 467.
- [10] P.B. Sunderland, G.M. Faeth, *Combust. Flame* 105 (1996) 132.
- [11] I. Glassman, *Proc. Combust. Inst.* 22 (1988) 295.
- [12] R.J. Santoro, T.T. Yeh, J.J. Horvath, H.G. Semerjian, *Comb. Sci. Tech.* 53 (1987) 89.
- [13] I. Glassman, *Proc. Combust. Inst.* 27 (1998) 1589.
- [14] J.D. Buckmaster, G.S.S. Ludford, *Theory of Laminar Flames*, Cambridge University Press, Cambridge, 1982, p. 95.
- [15] K. Mills, M. Matalon, *Comb. Sci. Tech.* 129 (1997) 295.
- [16] C.T. Avedesian, B.J. Callahan, *Proc. Combust. Inst.* 28 (2000) 991.
- [17] M.Y. Choi, K.-O. Lee, *Proc. Combust. Inst.* 26 (1996) 1243.
- [18] V. Nayagam, J.B. Haggard, Jr., R.O. Colantonio, A.J. Marchese, F.L. Dryer, B.L. Zhang, F.A. Williams, *AIAA J.* 36 (1998) 1369.
- [19] C.J. Sung, D.L. Zhu, C.K. Law, *Proc. Combust. Inst.* 27 (1998) 2559.
- [20] S.D. Tse, D. L. Zhu, C.-J. Sung, Y. Ju, C.K. Law, *Combust. Flame* 125 (2001) 1265.
- [21] D.X. Du, R.L. Axelbaum, C.K. Law, *Proc. Combust. Inst.* 22 (1988) 387.
- [22] D. Bradley, A.G. Entwistle, *Brit. J. Appl. Phys.* 12 (1961) 708.
- [23] S. Nakai, T. Okazaki, *Int. J. Heat Mass Transfer* 18 (1975) 387.
- [24] M.K. King, *Proc. Combust. Inst.* 26 (1996) 1227.
- [25] A. Atreya, S. Agrawal, *Combust. Flame* 115 (1998) 372.
- [26] M.M. Abu-Romia, C.L. Tien, *Trans. ASME* 89, Ser. C: *J. Heat Transfer* (1967) 321.
- [27] C.K. Law, *Prog. Energy Combust. Sci.* 8 (1982) 169.